ISSN 1810-2328, Journal of Engineering Thermophysics, 2017, Vol. 26, No. 2, pp. 197–215. © Pleiades Publishing, Ltd., 2017.

Modeling of Steady Herschel–Bulkley Fluid Flow over a Sphere

A. A. Gavrilov[1,2*], K. A. Finnikov[1,2], and E. V. Podryabinkin[2]

[1] *Institute of Thermophysics, Siberian Branch, Russian Academy of Sciences, Krasnoyarsk Branch, 50/44 Akademgorodok, ICM SB RAS, Krasnoyarsk, 660036 Russia*

[2] *Baker Hughes Inc., ul. Kutateladze 4a, Novosibirsk, 630090 Russia*

Received June 19, 2014

Abstract—Characteristics of the incompressible flow of Herschel–Bulkley fluid over a sphere were studied via systematic numerical modeling. A steady isothermal laminar flow mode was considered within a wide range of flow parameters: the Reynolds number $0 < \mathrm{Re} \leq 200$, the Bingham number $0 \leq Bn \leq 100$, and the power index $0.3 \leq n \leq 1$. The numerical solution to the hydrodynamic equations was obtained using the finite volume method in the axisymmetric case. The changes in flow structures, pressure and viscous friction distribution, and integral drag as a function of the flow rate and fluid rheology are shown. Depending on whether plastic or inertial effects dominate in the flow, the limiting cases were identified. The power law and Bingham fluid flows were studied in detail as particular cases of the Herschel–Bulkley rheological model. Based on the modeling results, a new correlation was developed that approximates the calculated data with an accuracy of about 5% across the entire range of the input parameters. This correlation is also applicable in the particular cases of the power law and Bingham fluids.

DOI: 10.1134/S1810232817020060

1. INTRODUCTION

The flow of an incompressible fluid over a sphere is a classic problem of hydrodynamics that has, on one hand, its own fundamental importance and, on the other hand, numerous practical applications. For example, the data regarding the parameters of these flows and hydrodynamic reactions on the sphere find direct application, for example, in a falling ball viscometer. Furthermore, these data can serve as the basis for description of more complex multiphase hydrodynamic processes such as sedimentation, fluidization, fluid transport, distribution of liquid and solid phases, etc. These processes find practical applications in various fields of technology, such as oilfield drilling, the chemical industry, food engineering and mineralogy. In these fields engineers need to know how flow carries a particle and the perturbations that result. There is an abundance of reported data on Newtonian fluid flows over a sphere [1, 2]. The drag coefficient dependence on the Reynolds number is of the greatest practical interest, and it is typically approximated by analytical expressions (correlations).

Knowledge of spherical particle movement in more complex rheological systems also has practical applications. Many of these systems fall into the general category of the so-called generalized Newtonian fluids. In this category the effective viscosity of the isothermal flows is determined by the local instant value of the second invariant of the strain rate tensor. The greatest proportion of these fluids can be categorized as pseudoplastic, where effective viscosity decreases when the shear rate increases, or viscoplastic, where yield stress must be exceeded to create a flow. Among the rheological models describing these fluids, the most common are the power law and Bingham plastic rheological models. It is no coincidence that most theoretical and experimental research related to non-Newtonian fluid flow over a sphere focuses on these rheological models.

At the same time, fluids exhibiting both pseudoplastic and viscoplastic properties are widely used, for example, in the oilfield drilling industry [4, 5]. One of the most common rheological models for these fluids is the Herschel–Bulkley rheological model, where the effective viscosity is expressed as follows:

* E-mail: gavand@yandex.ru

$$\begin{cases} \eta = \left(k\dot{\gamma}^{n-1} + \tau_0/\dot{\gamma}\right), & \tau \geq \tau_0, \\ \eta = \infty \quad (\dot{\gamma} = 0), & \tau < \tau_0. \end{cases} \tag{1}$$

Here, $\dot{\gamma} = \sqrt{1/2\dot{\gamma}_{ij}\dot{\gamma}_{ij}}$, $\tau = \sqrt{1/2\tau_{ij}\tau_{ij}}$ are second invariants of the strain rate tensor and the stress tensor, respectively; n, k, τ_0 are the rheological parameters of the Herschel–Bulkley model: power index, consistency index and yield stress. This rheological model is a combination of the power law and Bingham rheological models and coincides with them in particular cases where $\tau_0 = 0$ or $n = 1$, respectively.

When performing experimental studies of non-Newtonian fluids, it is necessary to measure the velocities of the sphere and fluid accurately, and to find the fluid rheological properties with high accuracy. In addition, there is the question of how accurately any rheological model can describe real fluids. Inaccurate representation of the fluid rheological behavior may cause poor agreement between theoretical and experimental results. The Herschel–Bulkley rheological model, as well as its particular cases, the power law and Bingham rheologies, is sometimes criticized in scientific literature for that very reason [5, 6]. However, these models are fairly simple and attractive. Consequently, they are widely used for practical applications and engineering studies. Within the framework of this theoretical research, we will not dwell on the aspects related to compatibility between the real fluid and its description by a selected rheological model. Instead, we focus on studying properties of the Herschel–Bulkley fluid flow. For the same reason, the results obtained will be compared with similar theoretical research.

In the case of the creeping flow of the power law fluid, there have been numerous attempts to solve this problem analytically. A vast survey of these studies is presented in a book by Chhabra [6], where it is noted that the results reported by different authors contradict each other and often do not agree with the experiment. The greatest discrepancy is observed for slow flows. In part, this may be due to the fact that the power law rheological model predicts infinite effective viscosity in the limit of the zero shear rate, which does not work well for slow flows of real fluids.

For Bingham fluids, the problem of slow flow over a sphere involves finding the critical force holding the sphere "fixed in" in the Bingham medium, i.e., finding the carrier properties of the fluids. Such a problem may have wide practical applications. The first attempts to solve this challenge used theoretical methods that were based on approximate analytical solutions. A detailed survey of these studies is also presented by Chhabra [6]. One of the first attempts to solve the equations for the Bingham fluid flow over a sphere with high accuracy and to obtain a flow field at low Reynolds numbers was made by Beris et al. [7]. Later, similar results were obtained using numerical modeling and reported in [8, 9].

Development of computational technologies in the end of the last century made it possible to study behavior of the power law and Bingham fluids at higher Reynolds numbers by solving hydrodynamic equations numerically. Systematic results for the drag obtained using numerical modeling are reported in [10–14] for the power index $n = 0.4 \div 2$ and Reynolds numbers up to $\mathrm{Re} = 500$. In [15] the effect of finite boundaries on the drag experienced by a sphere settling in quiescent power law fluids in cylindrical vessels has been investigated numerically. In papers [16, 17] concerning the heat transfer from heated sphere in Bingham [16] and Herschel–Bulkley fluid [17] the data for the drag coefficient are provided for selected flow regimes. At the same time to date, engineering application requires systematic data for the drag in a wide range of the flow parameters in Herschel–Bulkley fluid.

Our study has been motivated by the needs in accurate data for the drag coefficient within a wide range of Reynolds numbers and fluid parameters for a vast class of generalized Newtonian fluids. Our goal is the systematic modeling of the Herschel–Bulkley fluid flow over a sphere and the development of a universal and accurate correlation for finding the drag, based on the modeling results. A steady laminar flow within a wide range of Reynolds numbers and fluid parameters was considered. The statement of the problem is presented in detail in the next section. We used our own numerical algorithm for solving the hydrodynamic equations, based on the finite volume method [18, 19]. A brief description of the algorithm and verification of the computation method is provided in the second and third sections of this paper. Based on the modeling results obtained, an attempt was made to explain the formation of the flow structure and dependence of the flow parameters on the input data; see the fourth section. New correlations for the power law, Bingham, and Herschel–Bulkley fluids are presented in the fifth section.

2. STATEMENT OF PROBLEM AND NUMERICAL METHOD

The fluid flow is considered in the reference system associated with a sphere of the diameter d (radius r), located in an unbounded uniform fluid flow, whose velocity at a far distance from the sphere is U. The fluid has the density ρ and is a generalized Newtonian fluid with effective viscosity $\eta(\dot{\gamma})$ and Herschel–Bulkley rheological model (1). The steady isothermal flow of this fluid over a sphere is described by the hydrodynamic equations:

$$\nabla \cdot \mathbf{u} = 0,$$

$$\rho \mathbf{u} \cdot \nabla \mathbf{u} = -\nabla p + \nabla \cdot \boldsymbol{\tau}, \quad \boldsymbol{\tau} = \eta(\dot{\gamma}) \cdot \dot{\gamma}. \tag{2}$$

Here, $\mathbf{u}$ is the velocity vector, $\boldsymbol{\tau}$ is the strain rate tensor, $\dot{\gamma}_{ij} = \partial u_i/\partial x_j + \partial u_j/\partial x_i$, τ is the stress tensor.

In the general case for the problem of the flow over a sphere, it may be convenient to use the computational domain comprised of the space between two concentric spheres. The steady flow field is axisymmetric with respect to the axis parallel to the far field and passing through the center of the sphere. In addition, the computational domain is limited, with two planes crossing at this axis and creating a small angle. Thus, the computational domain is like a spherical slice with a sphere cut out in the center (see Fig. 1). The origin of the coordinates is in the center of the spheres, the axis x is directed along the flow, and the axis y is in the midsection, directed perpendicular to the far field flow.

The boundary conditions at the limiting planes are set as follows. On the surface of the outer sphere upstream of the sphere, $x < 0$ (1 in Fig. 1), the velocity of the unperturbed flow $\mathbf{u} = U\mathbf{e}_x$ is set, the velocity vector being directed along the axis x. On the surface of the outer sphere downstream from the sphere, $x > 0$ (2 in Fig. 1), the homogeneity condition is set for the flow along the axis x: $\partial \mathbf{u}/\partial x = 0$. On the surface of the solid sphere, the no-slip condition is set: $\mathbf{u} = 0$. At the sides of the computational domain, 4 in Fig. 1, the slip conditions are set for the flow: $\partial \mathbf{u}_\tau/\partial \mathbf{n} = 0$, $\mathbf{u}_\mathbf{n} = 0$.

The character of the flow is determined in its entirety by three dimensionless parameters: the power index n, the Reynolds number $\mathrm{Re} = \rho U d \Big/ k\dot{\Gamma}^{n-1}$, where $\dot{\Gamma} = U/d$ is the characteristic shear rate, and the Bingham number $Bn = \tau_0 \Big/ k\dot{\Gamma}^n$. During the course of systematic modeling, these parameters have been varied within the following ranges:

- Power index, $0.3 \le n \le 1$;
- Reynolds number, $0 < \mathrm{Re} \le 200$;
- Bingham number, $0 \le Bn \le 100$.

By computing the flow, the velocity and pressure fields are found, and the force acting on the sphere in the flow is calculated. This force has two components: $\mathbf{F} = \mathbf{F_P} + \mathbf{F_V}$, where the integral pressure force and viscous friction force are calculated via summation of pressure distributions $\mathbf{F_P} = -\int\limits_{surface} p\mathbf{n}dS$, $\mathbf{F_V} = \int\limits_{surface} \boldsymbol{\tau} dS$ and viscous stresses $\boldsymbol{\tau}$ on the surface of the sphere:

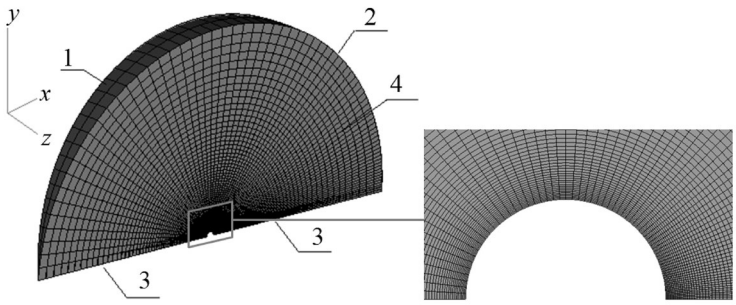

Fig. 1. The computational domain and grid.

$$\mathbf{F_P} = -\int\limits_{surface} p\mathbf{n}dS, \quad \mathbf{F_V} = \int\limits_{surface} \boldsymbol{\tau} dS.$$

The dimensionless drag coefficient is obtained dividing the corresponding integral force by the dynamic pressure of the unperturbed flow and the midsection area $S_m = \pi d^2/4$:

$$C_D = \frac{1}{S_m}\frac{\mathbf{F}}{\rho U^2/2}, \quad C_{D,P} = \frac{1}{S_m}\frac{\mathbf{F}_P}{\rho U^2/2}, \quad C_{D,V} = \frac{1}{S_m}\frac{\mathbf{F}_V}{\rho U^2/2}\,. \tag{3}$$

Thus, as a result of systematic modeling, we obtained the dependence of the drag coefficient on the flow parameters $C_D\,(n, \mathrm{Re}, Bn)$. Along with the drag (3), it is often convenient to present the results using a Y coefficient, thereby showing the difference from the Stokes formula:

$$Y\,(n, Bn, \mathrm{Re}) = C_D\,(n, Bn, \mathrm{Re})/(24/\mathrm{Re}),$$

$$Y_P\,(n, Bn, \mathrm{Re}) = C_{D,P}\,(n, Bn, \mathrm{Re})/(24/\mathrm{Re}), \quad Y_V\,(n, Bn, \mathrm{Re}) = C_{D,V}\,(n, Bn, \mathrm{Re})/(24/\mathrm{Re}). \tag{4}$$

The numerical algorithm is based on the finite volume method on unstructured grids. The details of its realization are described in [18, 19]. Its main features are listed below. The convective terms of the momentum equation are discretized using the second-order upwind scheme QUICK. The diffusive fluxes are discretized using a central differencing scheme with second-order accuracy. The relationship between the velocity and pressure fields that determine the continuity equations is realized using the SIMPLE-C procedure on collocated grids. This algorithm effectively couples the velocity and pressure fields by converting a discrete form of the continuity equation to an equation for the pressure correction. Oscillations of the pressure field are eliminated using the Rhie–Chow approach, which involves a special interpolation of the velocity at the faces of the control volumes. The linearized algebraic equations for transport equations are solved by preconditioned conjugate residuals methods. The system of algebraic equations obtained by discretization of the pressure correction equation is solved by an algebraic multigrid solver.

One of the difficulties with computing the viscoplastic medium flows via solving hydrodynamic equations with a variable effective viscosity is due to the infinitively high value of the effective viscosity in domains where the shear rate is zero. To overcome this difficulty, various regularization schemes have been developed for the original rheological models. The present paper uses the approach suggested by Papanastasiou [20], where approximating the smooth expression for effective viscosity in the case of the Bingham fluid flow is set by the following equation:

$$\eta\,(\dot{\gamma}) = \left[k\dot{\gamma}^{n-1} + \tau_0\left(1 - \exp(-m\dot{\gamma}\big/\dot{\Gamma})\right)\right]\big/\dot{\gamma}, \tag{5}$$

where m is nondimensional regularization parameter.

The selected computational domain allows for a fairly simple, structured C-type orthogonal grid (Fig. 1). The coordinate lines become denser toward the sphere, as well as in the circumferential direction downstream behind the sphere.

3. METHODICAL COMPUTATIONS AND VERIFICATION OF NUMERICAL METHOD

Systematic modeling was performed with the numerical algorithm parameters set as the same for all scenarios and with the same grid. For this reason, to find the values of these parameters with acceptable accuracy, several series of methodical precomputations were performed.

The calculated drag force acting on the sphere in the unbounded flow should be independent of the size of the computational domain. To find the size of the outer boundary that would have no significant influence on computation results, a series of methodical computations was performed for the outer boundary diameters of $25d$, $50d$, and $100d$. The computations were performed for Newtonian, power law ($n = 0.5$, $n = 0.3$), and Bingham fluids at $\mathrm{Re} = 0.01$, 10, and 100. The fluid that was the most sensitive to the computational domain size was the Newtonian fluid flow at low Reynolds numbers. In this case, the results may be compared not only with each other, but also with the analytical solution based on Stokes or Oseen. This comparison showed that the size of the computational domain with the outer boundary diameter $25d$ was insufficient. At the same time, for all fluids and flow modes, the differences with respect to the drag coefficient C_D calculated for the computational domains with diameters $50d$ and $100d$ did not exceed 1%. Consequently, the computational domain with the diameter $50d$ was selected for the systematic computations.

To check if the grid is sufficiently fine, computations on grids of different resolutions were performed. These computations showed that a grid with 110 nodes radially and 72 nodes circumferentially was acceptable. Computations on grids with higher numbers of nodes (doubled in each direction) did not have any significant effect on the result; the drag coefficient changed by no more than 1%.

Next, it was necessary to find a value of the regularization parameter m in Eq. (5) that would be acceptable for accuracy and speed. The higher the value, the closer the regularized model to the original. However, high values of this parameter slow down iterative convergence and inflate computation times. The test computations showed that $m = 1000$ is the optimal value of the regularization parameter. The drag coefficients obtained at a higher m did not differ by more than 1% in all modes.

To verify the results obtained, they were compared with the Schiller–Nauman correlation [21] for Newtonian fluids:

$$C_D = 24/\mathrm{Re}\left(1 + 0.15\mathrm{Re}^{0.687}\right). \tag{6}$$

This correlation, a classic in experimental research, has been confirmed to be accurate many times. The modeling results agreed well with this correlation; the discrepancy did not exceed 5%. Furthermore,

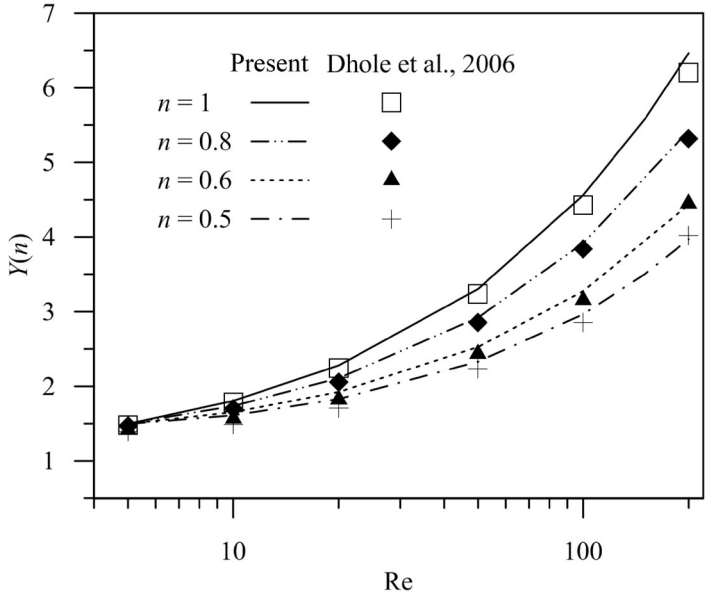

Fig. 2. Comparison of the results for coefficient Y (4) with the data from [11].

the computation results for the drag coefficient were compared with the data reported [11, 13, 15]. The comparison shows a good agreement for the drag coefficient. The discrepancy did not exceed 5% (see Fig. 2) across the entire range of Reynolds numbers and power indices, except for the slow flows where it reached 7%.

4. RESULTS AND DISCUSSION

4.1. Power Law Fluid

In the creeping flow mode (Re < 1), trajectories of the fluid particles before and behind the plane $x = 0$ are symmetrical for Newtonian and power law media. The symmetry of the velocity field is reflected in the distribution of effective viscosity of the power law medium (Fig. 3a). With the exception of local singularities, the greatest shear rate and the smallest effective viscosity are observed on the surface of the sphere. As the distance from the sphere increases, the shear rate drops and effective viscosity increases. The domains of minimal shear rate values and maximal viscosity values next to the sphere are localized in the neighborhood of critical points (next to the points of the axis Ox intersecting the sphere). The local viscosity maximum is in the ring-like domain around the sphere, slightly apart from it, where the low shear rate regions are formed.

As the power index decreases in the creeping flow mode, the shear rate increases on the surface of the sphere and decreases on the periphery (with the exception of local singularities in the critical points). At the same time, variations in the effective viscosity increase: the difference between its values at the sphere and on the periphery increases. Thus, the domain of the sphere's influence onto the flow decreases. At small power indices $n <\sim 0.4$, a high effective viscosity on the periphery could lead to a flow constraining. Its local velocity becomes higher than the velocity of the far field flow U (see Fig. 4b, dotted line), just like in the constrained flow over the particle (e.g., inside the pipe) [8]. This constraint boosts the difference between pressure values before and behind the sphere (see Fig. 5a) and increases the corresponding force component (see Fig. 6c). The input of the viscous forces behaves nonmonotonously with the increase of the power index n (see Figs. 5b and 6d): it is maximal at the power index close to $n = 0.7$. However, there is a force related to the nonuniformity of the pressure distribution over the sphere, and its relative contribution into the resulting drag force always increases with the decrease of the power index (see Fig. 6).

At moderate Reynolds numbers in power law and Newtonian fluid flows, inertial effects emerge. The symmetry of the streamlines with respect to the plane $x = 0$ disappears (see Figs. 3b and 3c), while the

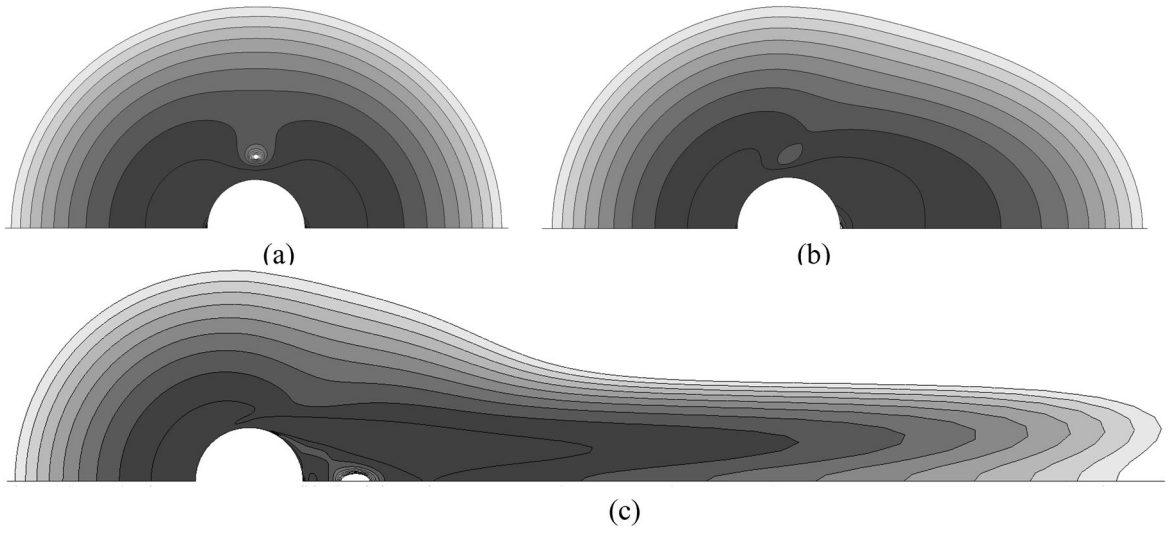

Fig. 3. Effective viscosity distribution for the medium with $n = 3$: (a) Re $= 0.1$; (b) Re $= 10$; (c) Re $= 100$. Isolines correspond to the gradual transition between two fixed values of effective viscosity $k\dot{\Gamma}^{n-1} \le \eta \le 10k\dot{\Gamma}^{n-1}$. The domains where the effective viscosity exceeds this range are shown white, the darker the lower the viscosity.

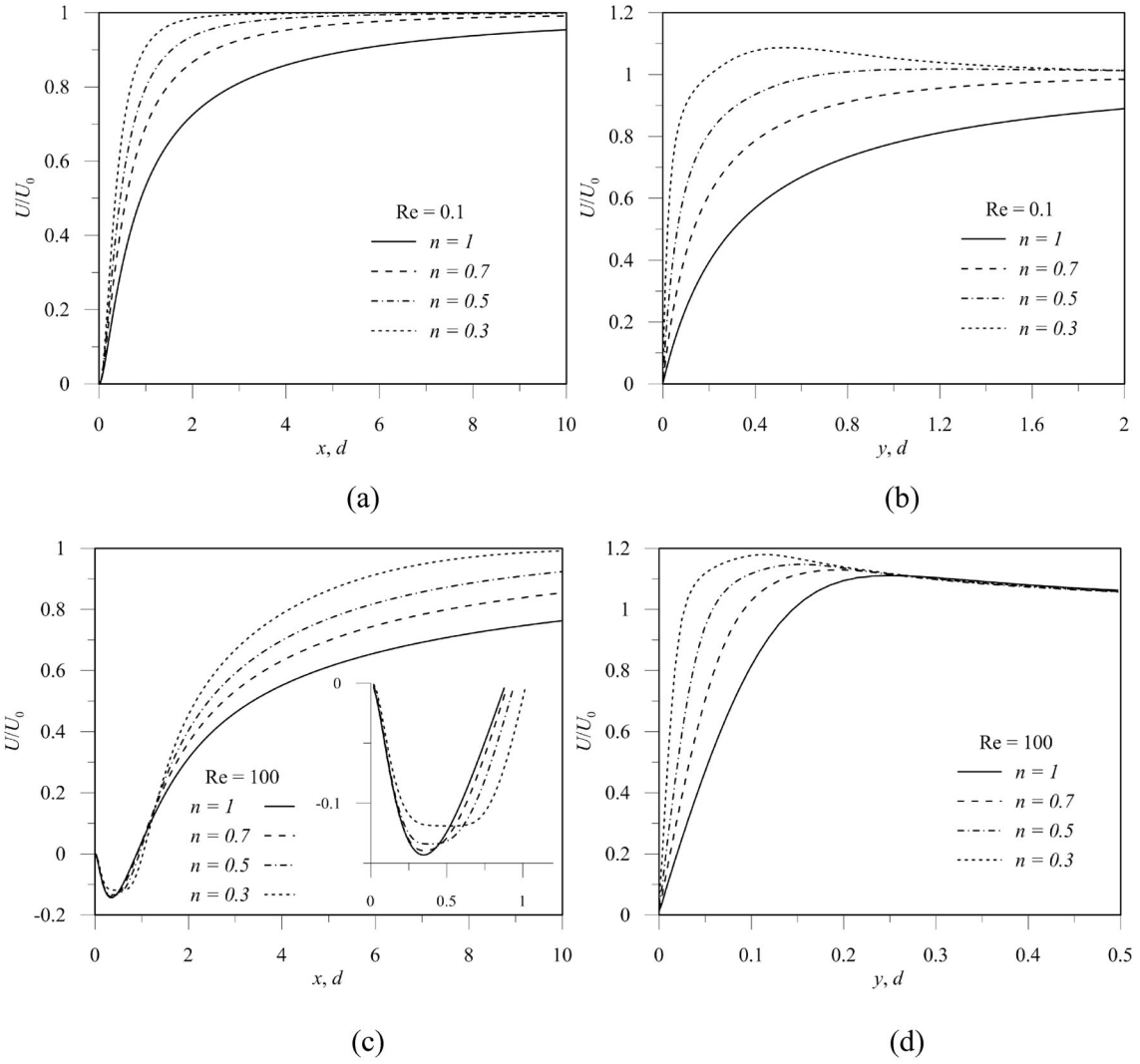

Fig. 4. Profiles of velocity components along Ox ((a), (c)), Oy ((b), (d)) for the power law medium at $\mathrm{Re} = 0.1$ ((a), (b)) and $\mathrm{Re} = 100$ ((c), (d)).

dependence of the drag on the Reynolds number deviates from $C_D \sim 1/\mathrm{Re}$, which is typical for creeping flows. The drag coefficient increases more slowly in the power law fluid than in the Newtonian fluid, see Fig. 6a. Dependence of the ratio of the drag coefficient for power law fluids to that of Newtonian fluid $C_D^n(\mathrm{Re})/C_D^{n=1}(\mathrm{Re})$ decreases monotonously at all $n < 1$, see Fig. 6b. It should be noted that all curved $Y^n(\mathrm{Re})$ for different power indices $n < 1$ with the computational accuracy intersect close to $\mathrm{Re} = 4$ (see Fig. 6b). However, dependences of the drag coefficient due to pressure $C_{D,P}(n, \mathrm{Re})$ and viscous components $C_{D,V}(n, \mathrm{Re})$, for different n have no notable features close to this value (see Figs. 6c, 6d). Furthermore, the nonmonotonous dependence of the drag component $C_{D,V}(n, \mathrm{Re})$, related to viscous stress upon n at low Reynolds numbers increases monotonously at high Reynolds numbers (see Fig. 6d). Viscous friction in fluids whose rheology is considerably non-Newtonian ($n \sim 0.3$) only weakly depends on Reynolds numbers (see Fig. 6d, dotted line). This situation is not typical of Newtonian fluids, where viscous friction increases with the increase of Re. The main contribution is due to the component related to pressure distribution over the sphere; this component increases monotonically, but more slowly than in the case of Newtonian fluids.

Just as in the case of Newtonian fluids, an axisymmetric toroidal vortex forms behind the sphere at high Reynolds numbers (see Fig. 4c). However, in the case of power law fluids, the streamlines become denser toward the sphere with the decrease of n due to high viscosity on the periphery that

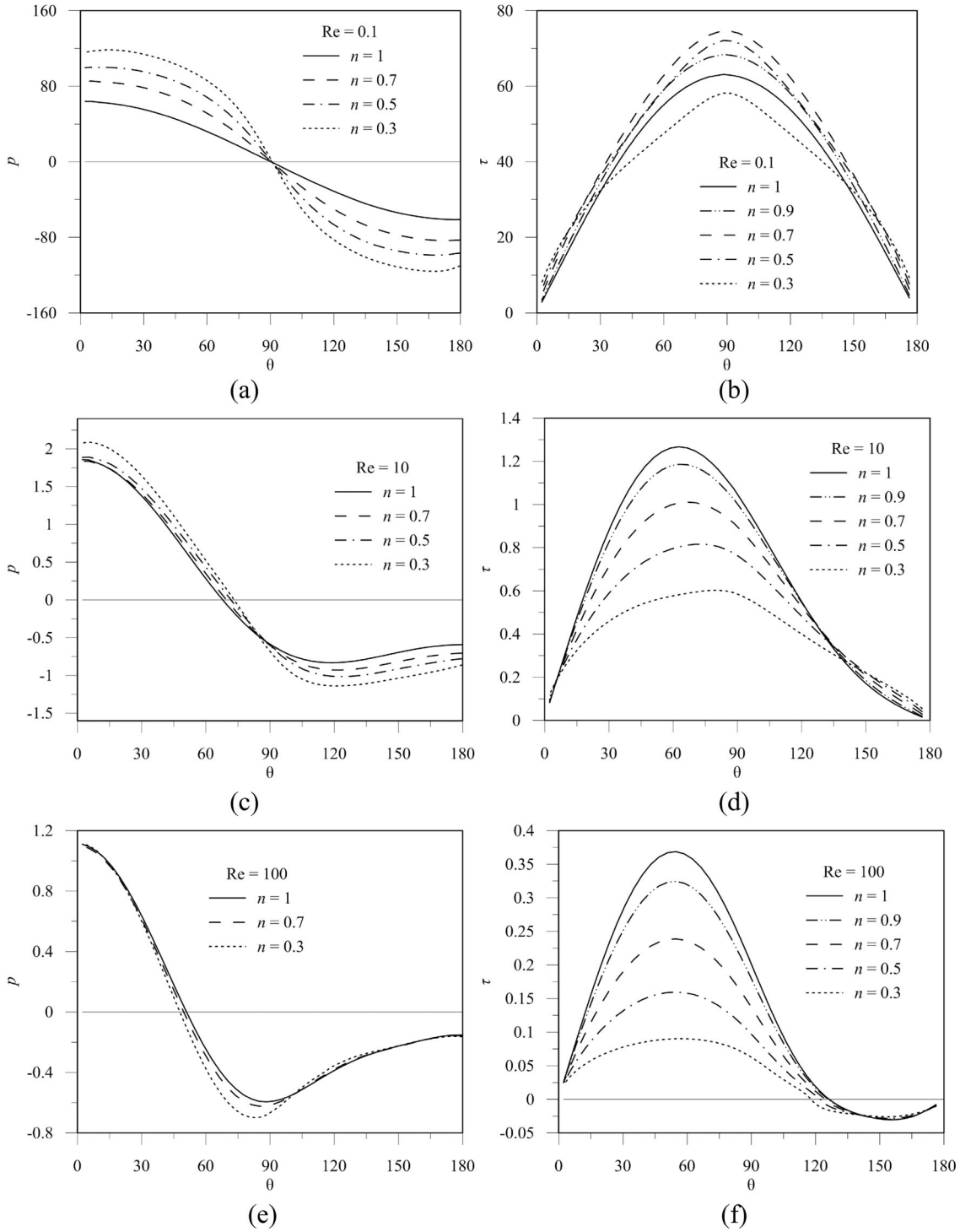

Fig. 5. Distributions of pressure ((a), (c), (e)) and tangent stress ((b, (d), (f)) on the surface of the sphere for the power law fluid: (a), (c) Re = 0.1; (b), (d) Re = 10; (e), (f) Re = 100.

effectively constrains the flow. As a result, the detaching point on the surface of the sphere shifts slightly upstream, and the toroidal vortex changes shape. With the decrease of the power index n, the length of the recirculation region behind the sphere increases, but homogeneity in the wake behind the toroidal vortex restores in a shorter distance (see Figs. 3c and 4c). This behavior is due to the difference in effective viscosity in the toroidal vortex, where it is relatively low due to a high shear rate, as opposed to

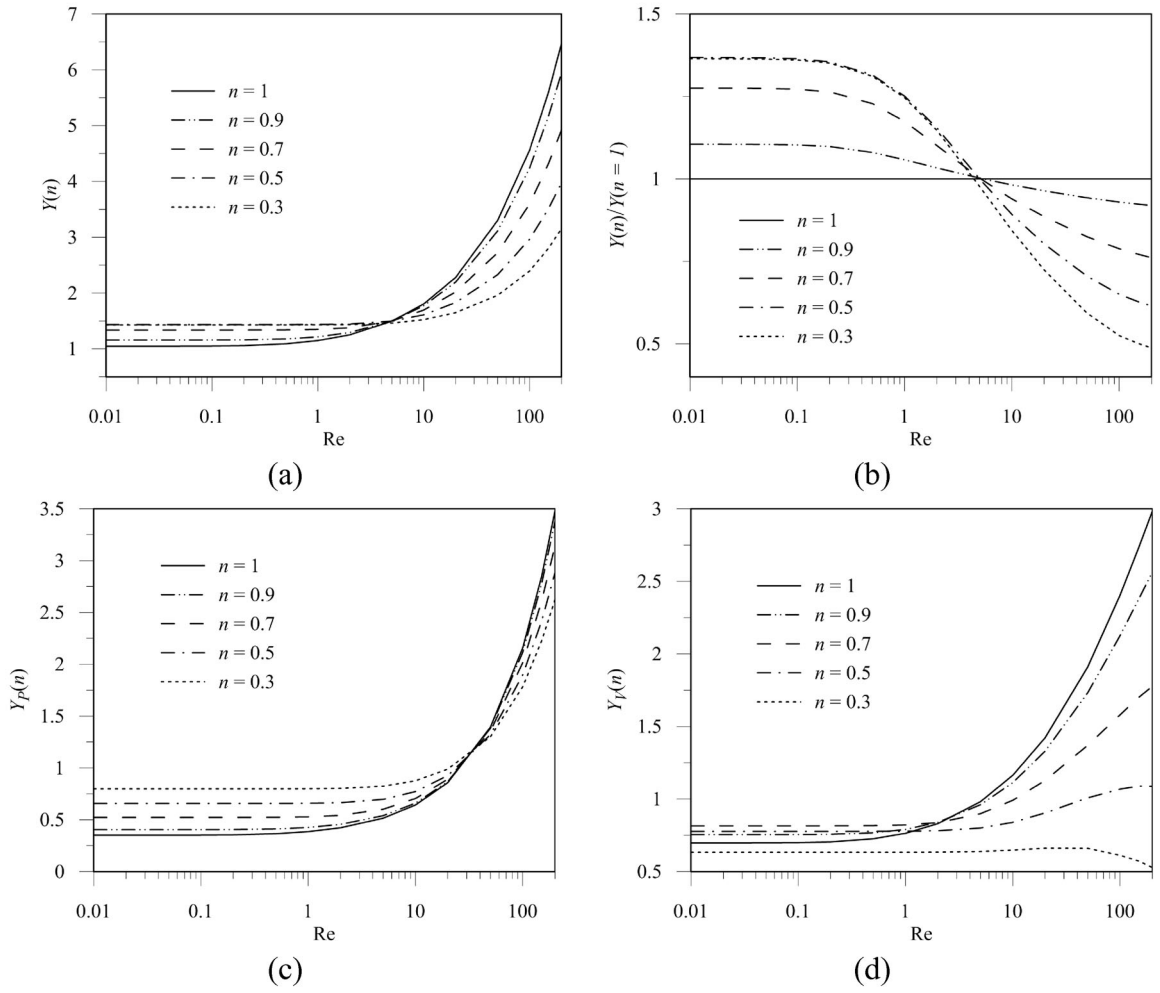

Fig. 6. Dependence of the coefficient Y (a), ratio of the drag coefficient for power law to that of Newtonian fluid (b), and the components of the drag coefficient Y_P, due to viscous pressure (c) and viscous friction Y_V (d) dependence on the Reynolds number in the power law fluid.

the wake behind the sphere on the axis of symmetry, where it is relatively high due to a low shear rate. Therefore, the disturbed region introduced by the sphere shrinks with the decrease of power index.

4.2. Bingham Fluid

A feature of fluids with yield is the formation of rigid-like areas within the flow, where the flow has no strain rate and the medium behaves like a solid body. When the uniform flow meets a sphere, a liquid region forms around it, while on the periphery the medium translates with no shear rate. In the creeping flow mode, the liquid region is symmetrical with respect to the plane $x = 0$ (see Fig. 7a). Generally, the flow structure and some of its features for the creeping flow mode are described in [7, 8].

With the increase of the Bingham number, which characterizes the influence of plastic effects, the size of the liquid region around the sphere decreases while the streamlines become denser toward the sphere (see Figs. 8a and 8b). At the same time, just as in the power law medium at low n, the flow is restricted by the boundaries of the rigid area on the periphery, and as a result, local velocity of the flow next to the sphere increases, i.e., the flow around the sphere is locally faster than the undisturbed flow (see Fig. 8b). With the increase of the yield stress and Bingham number, not only the size of the liquid region decreases, but also the viscous stress increases, if the shear rate inside the liquid region remains the same ($\tau = k\dot{\gamma} + \tau_0$). It may be obvious that this enhances the carrier properties of the fluid and the drag (see Fig. 9). Dependence of the drag on the Bingham number $C_D\,(Bn)$ is almost linear at high Bn.

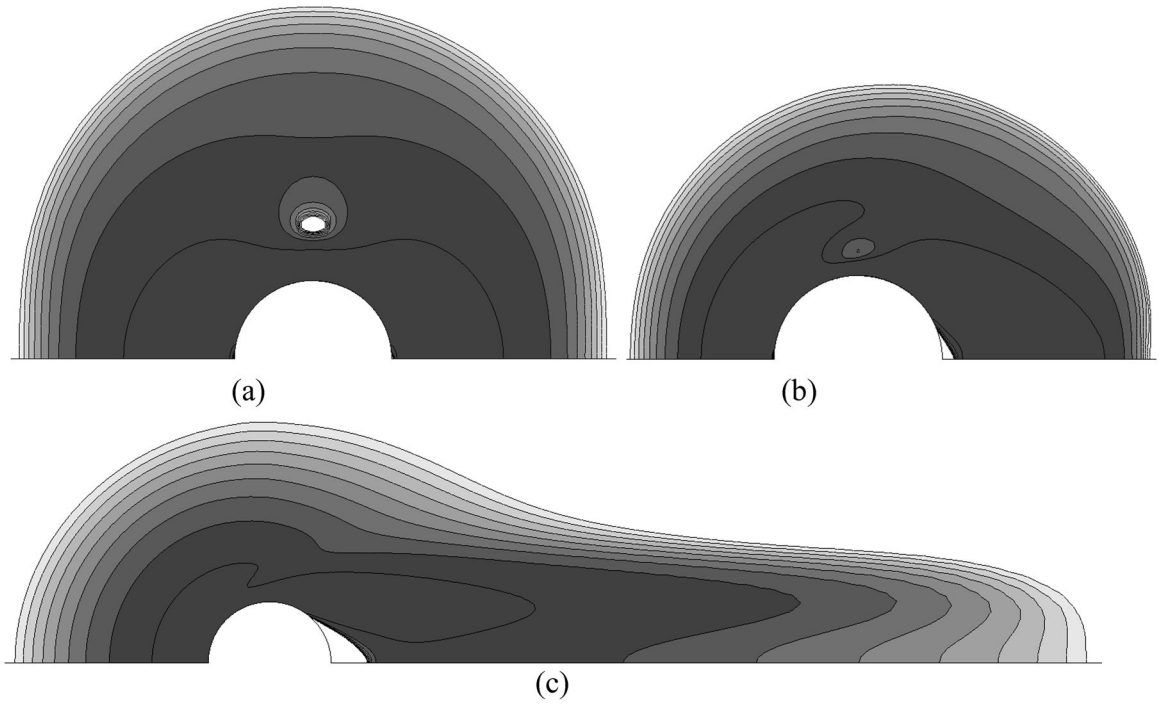

Fig. 7. Effective viscosity distribution for Bingham fluid: (a) $\mathrm{Re} = 0.1$, $Bn = 1$; (b) $\mathrm{Re} = 100$, $Bn = 10$; (c) $\mathrm{Re} = 100$, $Bn = 1$. Isolines correspond to gradual transition between two fixed values of effective viscosity $k(1 + Bn) \leq \eta \leq 10k(1 + Bn)$. The domains where the effective viscosity exceeds this range are shown white, the darker the lower the viscosity.

The Bingham fluid flow at moderate Reynolds numbers is defined by the ratio between the Bingham number Bn and the Reynolds number Re. Two limiting cases may be identified here: (1) plastic effects in the flow are weak ($\mathrm{Re}/Bn >\sim 100$); (2) plastic effects in the flow dominate ($\mathrm{Re}/Bn <\sim 10$).

In the first case, the liquid flow region over the sphere is fairly large, and the flow field is generally similar to the one observed in the case of the Newtonian fluid. With the increase of the Reynolds number at a fixed Bn, the difference between the Bingham fluid flow and the Newtonian fluid flow becomes negligible. This is evident from the velocity profiles (Fig. 8). At high Re and low Bn, they basically coincide with the Newtonian case, see dashed and solid lines in Figs. 8c and 8d, even though they differ significantly at low Re for the same Bn, see dashed and solid Figs. 8a and 8b. Velocity distributions, see Fig. 8, clearly demonstrate that evolution of inertial effects in the flow due to an increase in the Reynolds number, even at a fixed Bingham number, in Newtonian and Bingham fluids occurs similarly: first, the symmetry of the streamlines with respect to the plane $x = 0$ breaks, and when Re increases further, a toroidal vortex is formed in the wake behind the sphere.

The kinematic picture of the flow over the sphere for the case of $\mathrm{Re}/Bn >\sim 100$ is similar to Newtonian, while the effective viscosity $\eta\,(\dot{\gamma}) = [k\dot{\gamma} + \tau_0]/\dot{\gamma}$ seems to remain basically unchanged next to the sphere. Hence, the distributions of pressure and viscous stress over the sphere in the cases of Newtonian and Bingham fluids are also similar (see Figs. 10e and 10f, the lines corresponding to $Bn \leq 1$). However, the drag is higher than in the case of Newtonian fluid (see Fig. 9) because the effective viscosity in Bingham fluid is higher in the liquid regions due to nonzero yield stress. It should be noted that, for a real Bingham fluid, an increase in the flow velocity not only boosts the Reynolds number, but also diminishes the Bingham number. This is due to dependence on the velocity U. Thus, unlike dependences Y (Re) shown in Figs. 9a, 9b for fixed Bingham numbers, an increase in the flow velocity causes the drag in Bingham fluid approach the drag in Newtonian fluid with the same viscosity μ (whereas its dependences on the Reynolds number at different Bn shown in Figs. 9a, 9b are basically parallel).

In the second limiting case ($\mathrm{Re}/Bn <\sim 10$), the flow field is determined by plastic effects that intensify with the increase of Bn at a fixed Re. The liquid region shrinks in this case, but the effective

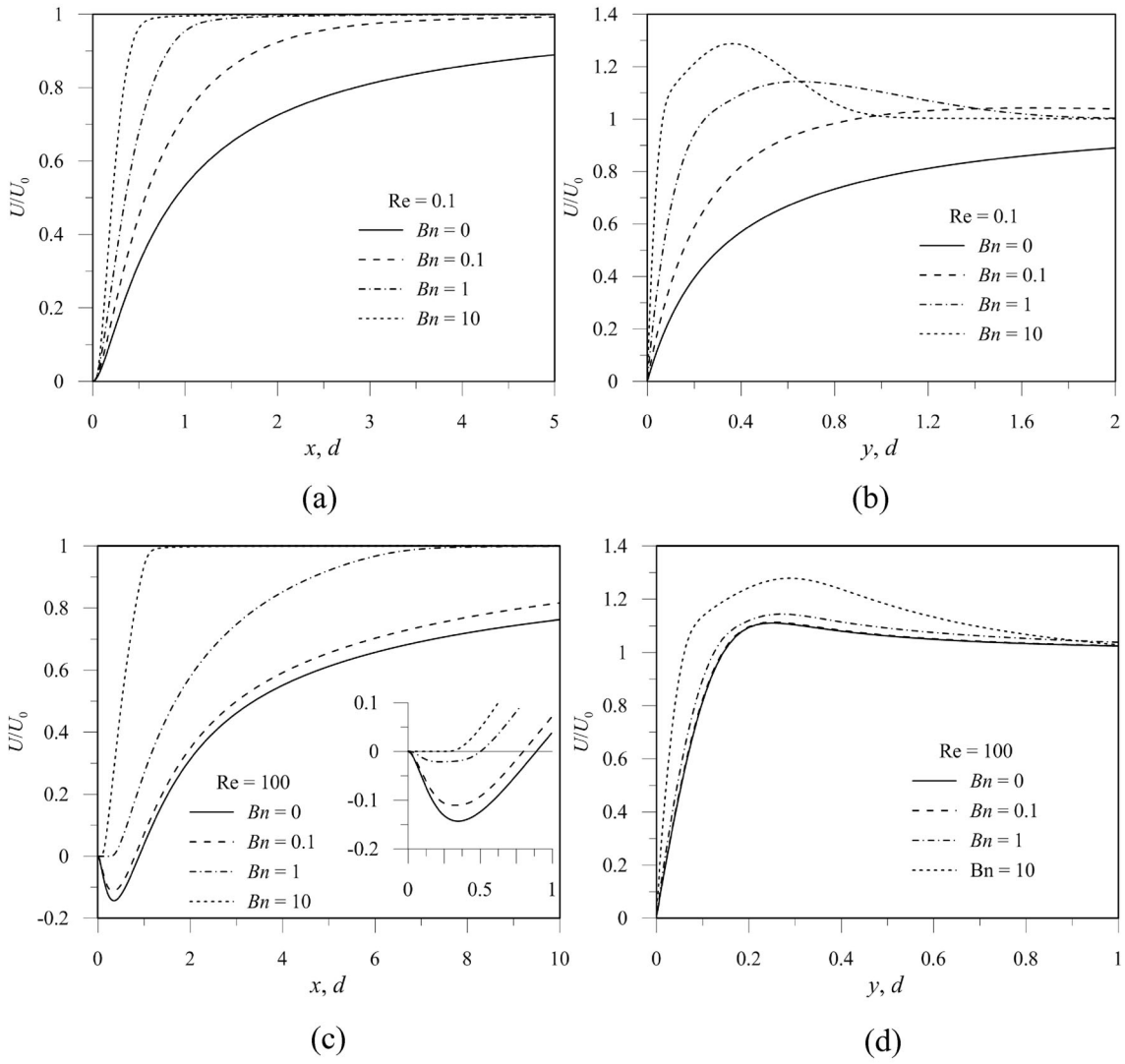

Fig. 8. Profiles of velocity components along Ox ((a), (c)), Oy ((b), (d)) for Bingham fluid $\mathrm{Re} = 0.1$ ((a), (b)) and $\mathrm{Re} = 100$ ((c), (d)).

viscosity inside this region increases. This suppresses inertial effects in the fluid flow. For this reason, with the increase of the Bingham number, the flow field around the sphere becomes close to the creeping flow without the flow detaching, even at high Re. For fluids with $Bn > 10$, even at $\mathrm{Re} = 100$, the toroidal vortex behind the sphere does not form, see Fig. 7b, the dotted line in Fig. 8c. The lower the ratio Re/Bn, the closer the kinematic pattern of the flow over the sphere to that of a creeping flow. For this reason, distributions of pressure and viscous friction on the surface of the sphere become practically symmetrical, even at relatively high Reynolds numbers (cf. two-dot-dashed line in Figs. 10c, 10d with the lines in Figs. 10a, 10b, respectively). Thus, the drag coefficient $Y(\mathrm{Re}, Bn)$ is determined almost exclusively by the Bingham number and basically does not depend on the Reynolds number (see Fig. 9a). In this mode, the drag force is proportional to the far field flow velocity. It should be noted that, in the classical creeping mode, the viscous forces dominate over the pressure forces, while in the cases of flows with high Bn, the pressure forces dominate over the viscous forces.

The modeling results for Bingham fluid show that, for $Bn \ll \mathrm{Re}$, the following limit is realized:

$$Y = \frac{\mathrm{Re}}{24} C_D \to \mathrm{const} \cdot Bn, \tag{7}$$

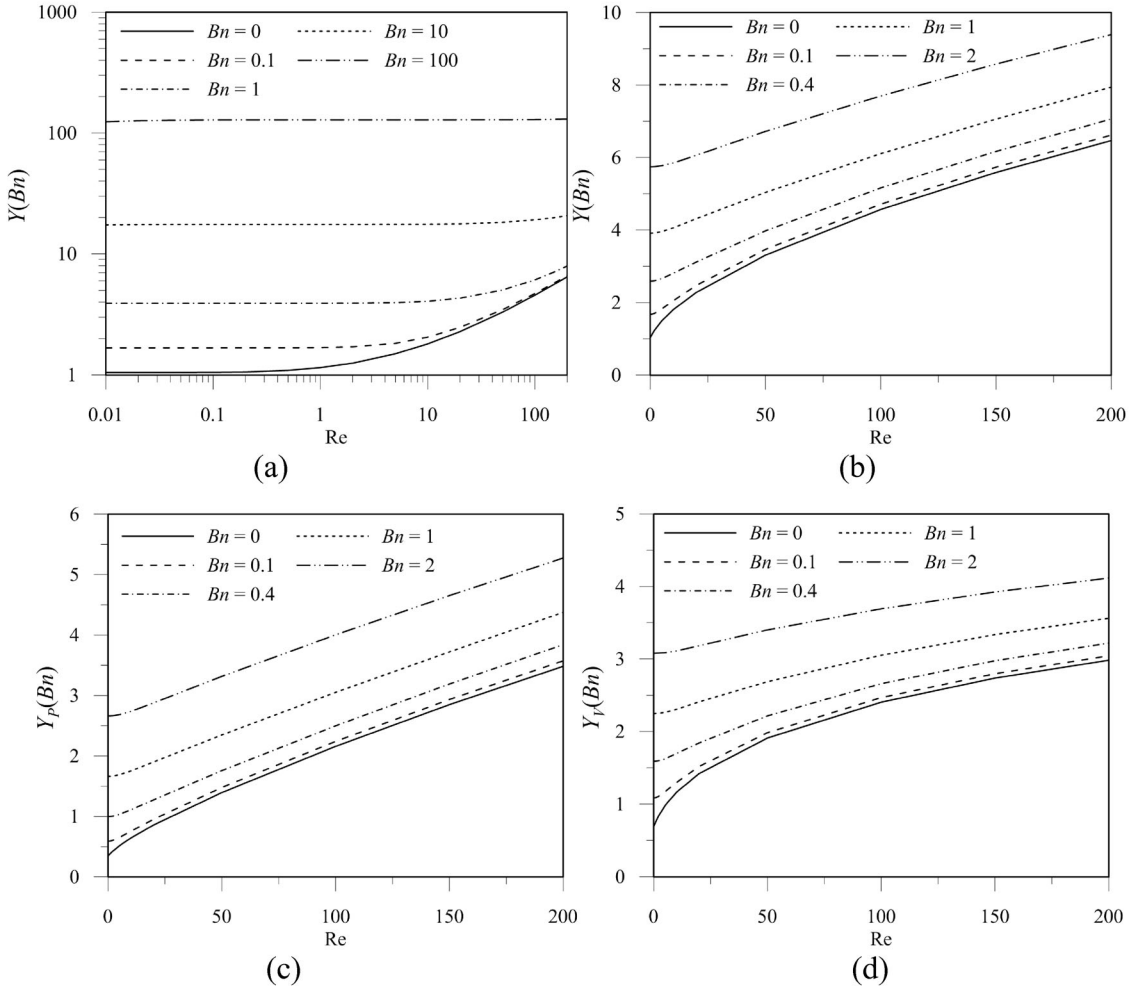

Fig. 9. Dependence of Y (log scale: (a) normal scale: (b)) and drag (pressure components Y_P: (c), and friction components Y_V: (d)) on the Reynolds number at different Bingham numbers.

which matches perfectly the plastic flow over the sphere. At $Bn = 100$ the calculated constant in (7) is 1.24, whereas at $Bn = 500$ the value of this constant reported in [7] is 1.17. Asymptotic dependence (7) reflects the finite nonzero value of the drag force in the limit of the zero velocity of the particle with respect to the flow.

Between the two described limiting cases, there is a range of Bingham numbers and Reynolds numbers where the role of plastic, viscous, and inertial forces is comparable. Here, an increase of the Bingham number leads to an increase in plastic effects, the size of the liquid regions decreases, the vortex formation behind the sphere is suppressed, and as a result, the drag increases. On the other hand, an increase in the Reynolds number at a fixed Bingham number, leads, first, to the flow detaching on the sphere and to formation of a toroidal vortex in the wake behind the sphere. This scenario develops the vortex and increases the size of the liquid domain in the wake behind the sphere. Unlike in a Newtonian fluid, a rigid-like region is formed behind the sphere on the axis of symmetry, right next to the sphere. The flow over the sphere now looks like a flow over an oblong body, whose longer side is oriented along the flow (see Fig. 7c). Compared to Newtonian fluid, the detaching point on the sphere is shifted slightly downstream, and the size of the vortex is smaller. In the recirculation domain, effective viscosity is higher than in the shear flow over it, while the length of the perturbation wake in the flow is shorter. With the increase of Re at fixed Bn, the contribution of the pressure forces increases, while the ratio of viscous forces to pressure forces tends to the value for Newtonian fluids.

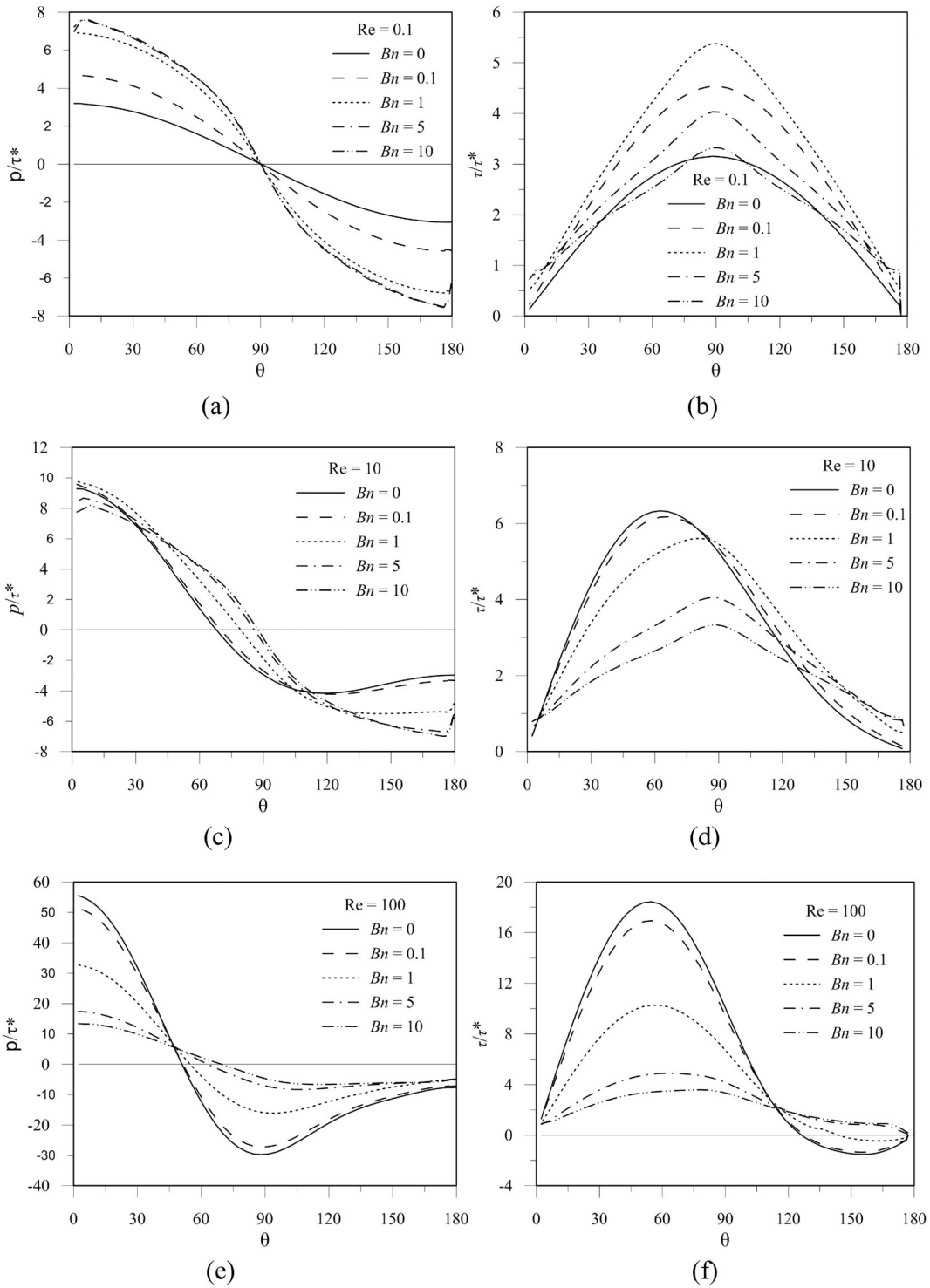

Fig. 10. Distributions of pressure ((a), (c), (e)) and tangent stress ((b), (d), (f)) over the surface of the sphere in the Bingham fluid flow at different Reynolds numbers.

4.3. Herschel–Bulkley Fluid

The Herschel–Bulkley fluid model incorporates the power law and Bingham models, combining their behavior. Thus, features of the power law and Bingham fluids flow are shared by the Herschel–Bulkley fluid flow. The influence of the power index and the Bingham number on the flow parameter is similar. For this reason, we will discuss only those features of the flow over the sphere for this case that were not described above.

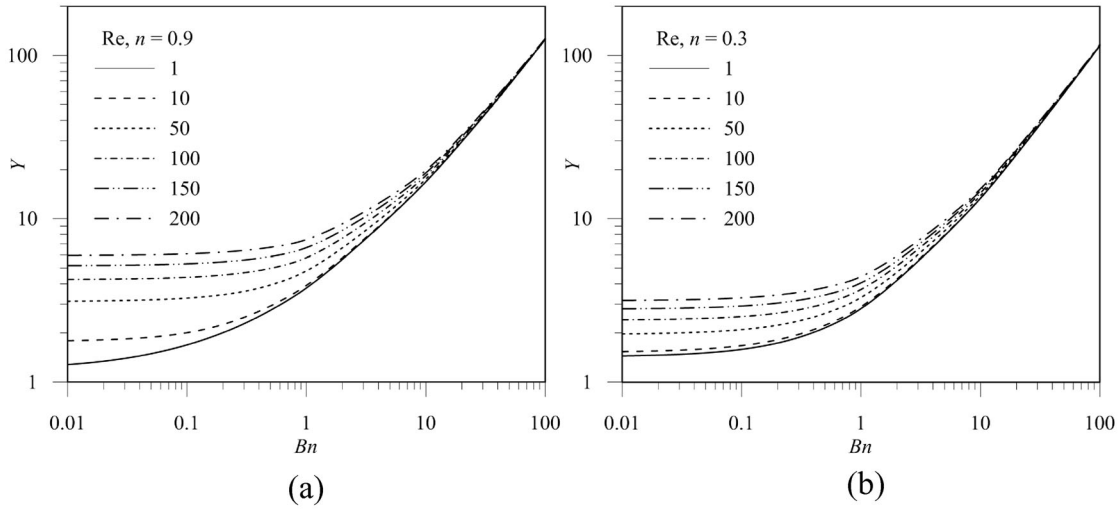

Fig. 11. Dependence of Y on the Bingham number for different Reynolds numbers in Herschel–Bulkley fluid: (a) $n = 0.9$; (b) $n = 0.3$.

As in the case of the Bingham fluid, when there is a flow over the sphere, a liquid region is formed around the sphere, whereas on the periphery the medium behaves as a rigid substance. The size of the liquid region is determined primarily by the Bingham number: the higher the Bingham number, the smaller the liquid region. At the same time, its size also depends on the power index: the lower the power index, the smaller the liquid region. Therefore, one could conclude that the perturbations introduced to the flow by a sphere diminish when the fluid rheology becomes more non-Newtonian, if the Bingham number is higher and/or the power index is lower. In highly non-Newtonian fluids, dependence of the drag and kinematic characteristics of the flow on the Reynolds number is weaker than in Newtonian fluids. Sensitivity of the flow properties to changes in the relative velocity weakens with the increase of non-Newtonian fluid properties (see Fig. 11).

Just as in the case of Bingham fluids, at high Bingham numbers and moderate Reynolds numbers, the so-called plastic limit is realized, where dependence of kinematic and dynamic flow properties on the Reynolds number is practically nonexistent (see Fig. 11). In this case, the viscous stress in the fluid is much lower than plastic, and the flow properties are practically the same in the fluids with any power index.

5. CORRELATIONS FOR DRAG COEFFICIENT

The development of an approximate analytical correlation for finding the drag coefficient is one of the goals of our study. Such a formula may be used in engineering applications for finding the drag force at a given relative particle velocity with respect to the fluid. Here we present the correlation for power law fluid. Next, involving analysis of the flow behavior a formula describing drag in plastic flow regime is derived. Then these expressions are combined and corrected to obtain the correlation for the drag coefficient in Herschel–Bulkley fluid.

A correlation for the drag coefficient in the power law fluid was derived by generalizing the well-known Schiller–Nauman correlation [21] for the drag in Newtonian fluid (6). For this purpose we replaced the constants in this formula with the polynomic functions of the second degree of the reverse power index parameter $\tilde{n} = 1 - n$:

$$C_D = 24 Y_{PL}\,(\mathrm{Re}, n)/\mathrm{Re};$$

$$Y_{PL}\,(\mathrm{Re}, n) = 1 + C_{PL1}\tilde{n} + C_{PL2}\tilde{n}^2 + \left(0.15 + C_{PL3}\tilde{n} + C_{PL4}\tilde{n}^2\right) \mathrm{Re}^{0.687 + C_{PL5}\tilde{n} + C_{PL6}\tilde{n}^2}. \quad (8)$$

The coefficients $C_{PL1}, \ldots, C_{PL6}$ were found by minimization of the functional of deviation between calculated values, Y^{calc} and their approximation (8), Y^{app}:

$$\Phi = \sum_i \left\{ \ln \left[Y^{calc} \left(\mathrm{Re}_i, n_i \right) \right] - \ln \left[Y^{app} \left(\mathrm{Re}_i, n_i \right) \right] \right\}^2. \quad (9)$$

Here, summation is performed over all the modeled flow scenarios. This form of the functional was selected to enable minimization of the mean relative deviation of the approximation from the computation results using Levenberg–Marquardt algorithm [22]. As a result of minimization of (9), the following values for the coefficients in dependence (8) were obtained:

$$C_{PL1} = 1.375,\ C_{PL2} = -1.11,\ C_{PL3} = -0.309,\ C_{PL4} = 0.17,\ C_{PL5} = 0.131,\ C_{PL6} = 0.193. \quad (10)$$

With these coefficients, the maximal relative deviation of (8) from calculated results is 3.9%. Formula (8) with values (10) is the correlation for the drag coefficient in power law fluids and can be used for determination of the drag force on a sphere.

To extend correlation (8) for the case of yield stress fluids drag behavior in the plastic flow regime is required to be described. Analysis of Bingham fluid flow over sphere performed by Beris et al. [7] yields the following form of asymptotic dependence of Y in the limit of high Bingham numbers:

$$Y = \frac{\mathrm{Re}}{24} C_D = \mathrm{const}_1 \cdot Bn + \mathrm{const}_2 \cdot \sqrt{Bn}. \quad (11)$$

Such form of dependence is more accurate than (7) at moderate Bingham numbers. Dependence (11) can be generalized for the case of Hershel–Bulkley taking into account the following mechanical reasoning. When there is a force slightly greater than critical acting on the particle, the fluid begins to flow in the region where the shear stress is higher than the yield. The shear stress caused by the force acting on the particle decreases with the distance from the particle surface, and at the distance of approximately one particle diameter the stress loses much of its value. Consequently, the characteristic thickness of the layer next to the particle, where the shear stress is higher than the yield, is as follows:

$$h \sim d \left(\frac{F}{F_0} - 1 \right),$$

where F_0 is the yielding drag force. When drag force is close to yielding $F/F_0 - 1 \ll 1$ and $h \ll d$, the law of shear stress decrease is close to linear, which can be written as

$$\tau(x) - \tau_0 \sim \frac{F - F_0}{d^2} \left(1 - \frac{x}{h} \right),$$

where x is the distance from the sphere. The velocity of the particle is estimated as integral of shear rate over the distance from sphere:

$$u \sim \int_0^h \gamma(\tau(x))\, dx \sim (F - F_0)^{\frac{n+1}{n}} k^{-1/n} F_0^{-1} d^{1-2/n}.$$

Thus, we have the following expression for the Stokes coefficient:

$$Y = \frac{F}{\rho U^2 \pi d^2/8} \frac{\rho U^{2-n} d^n}{k} = \mathrm{const}_1 \cdot Bn + \mathrm{const}_2 \cdot Bn^{\frac{n}{n+1}}. \quad (12)$$

In the case of Bingham fluid, $n = 1$, this dependence coincides with (11). With the properly chosen constants this dependence reproduces asymptotic behavior of drag with a high accuracy. Approximation error in our tests does not exceed 3% within the range $0.3 \le n \le 1$, $\mathrm{Re} < 1$, $Bn > 10$.

The correlation for the drag in Herschel–Bulkley fluid as a function of Re, Bn, and n can be obtained by combination of dependence describing plastic flow regime (12) with the correlation for power law fluid (8), (10)

$$C_D = 24Y_{HB}/\mathrm{Re}; \quad Y_{HB} = Y_{PL}\left(\mathrm{Re}, n\right) + \mathrm{const}_1 \cdot Bn + \mathrm{const}_2 \cdot Bn^{\frac{n}{n+1}}.$$

This expression accurately approximates the drag coefficient in the limiting cases of high and very low Bingham numbers. However, for an accurate approximation in the intermediate range of Bingham numbers it should be modified, taking into account the effects of the toroidal vortex suppression behind the sphere in the yield stress fluids. An approach to describing this effect while developing correlations was proposed in [23] and further advanced in numerous subsequent publications; it is based on introducing the so-called dynamic parameter

$$Q = \frac{\mathrm{Re}}{1 + Bn} \tag{13}$$

and developing its correlational dependence. This parameter is substituted instead of Reynolds number, leading to the following drag coefficient approximation:

$$C_D = \frac{24}{\mathrm{Re}} Y_{HB}\left(Q, Bn, n\right),$$

$$Y_{HB}\left(\mathrm{Re}, Bn, n\right) = Y_{PL}\left(Q\left(\mathrm{Re}, Bn\right), n\right) + C_{HB1}(n) \cdot Bn + C_{HB2}(n) \cdot Bn^{\frac{n}{n+1}}. \tag{14}$$

The method of finding coefficients $C_{HB1}(n)$, $C_{HB2}(n)$ in this dependence is the same as in case of the power law fluid. However, accuracy of approximation of modeling results by expression (14) was about 11%. Obviously, introduction of dynamic parameter in the form (13) does not allow describing of coupled influence of Bingham and Reynolds numbers on the Stokes coefficient in the whole parameters range. To improve the approximation accuracy of (14), a more general form of the dynamic parameter (13) is required:

$$Q\left(\mathrm{Re}, Bn, n\right) = \frac{\mathrm{Re}}{1 + C_{HB3}(n) Bn^{C_{HB4}(n)} \mathrm{Re}^{C_{HB5}(n)}}. \tag{15}$$

With this form of dynamic parameter, the approximation error for the calculated data has been reduced to 5%. The polynomic functions of second degree $C_{HB1}(n), \ldots, C_{HB5}(n)$ were found by minimization of functional (9):

$$\begin{aligned}
C_{HB1}\left(n\right) &= 1.09 - 0.3\tilde{n} + 0.214\tilde{n}^2, \\
C_{HB2}\left(n\right) &= 1.79 - 2.64\tilde{n} + 0.909\tilde{n}^2, \\
C_{HB3}\left(n\right) &= 28.6 + 18.3\tilde{n} - 68.9\tilde{n}^2, \\
C_{HB4}\left(n\right) &= 0.566 - 0.01\tilde{n} - 0.384\tilde{n}^2, \\
C_{HB5}\left(n\right) &= -0.73 - 0.464\tilde{n} + 0.045\tilde{n}^2,
\end{aligned} \tag{16}$$

where $\tilde{n} = 1 - n$. These values coincides with (10) at $n = 1$.

Correlation (14), (15) with (16) and (10) is continuous, smooth and universal for Herschel–Bulkley fluids and can also be applied to Bingham and power law fluids. The approximation error for the calculated data does not exceed 5% in the range $0.3 \le n \le 1$; $0 < \mathrm{Re} \le 200$; $0 \le Bn \le 100$. One of the advantages of this formula is the correct approximation of the drag force in plastic flow regime (at high Bingham numbers). In particular, it yields a value of 1.17 for the constant in (7) at $Bn = 500$, which perfectly agrees with the results reported in [7].

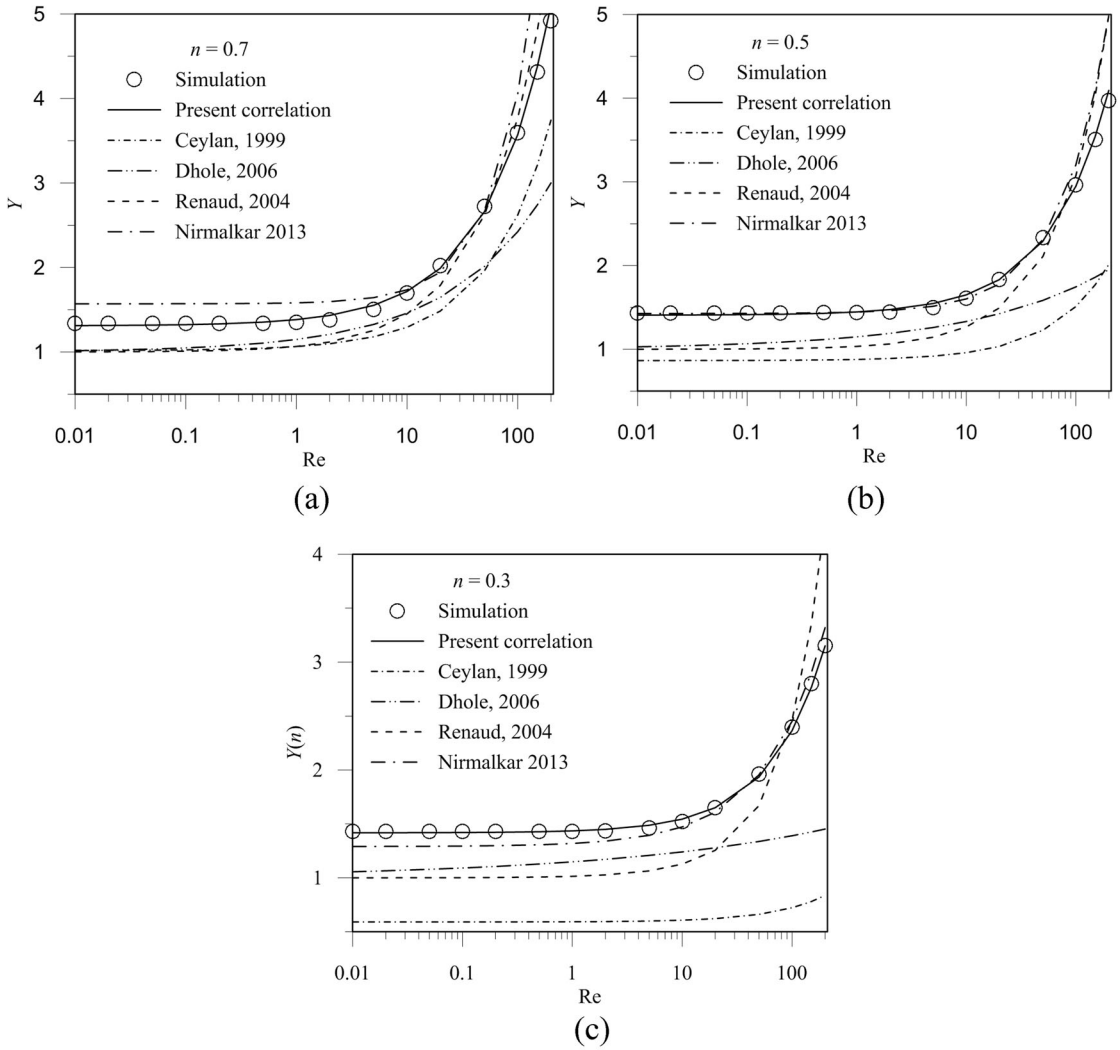

Fig. 12. Comparison of $Y(\mathrm{Re}, n) = C_D(\mathrm{Re}, n)/C_D(\mathrm{Re}, 1)$ calculated via different correlations for the power law fluid: (a) $n = 0.7$; (b) $n = 0.5$; (c) $n = 0.3$.

Dependence of the calculated drag on the Reynolds number and power index was compared with several known dependences obtained via theoretical analysis or experiment [13, 17, 24, 25]. The comparison results for the power law fluid are shown in Fig. 12 as dependences of $Y\,(\mathrm{Re}, n) = C_D\,(\mathrm{Re}, n)/C_D\,(\mathrm{Re},\,1)$ on the Reynolds number. The lines in the figures correspond to existing correlations (only the correlations most similar to our computations are shown in the figures), and points correspond to the modeling results. Comparison of the modeling results for the power law fluid with known empirical dependences shows that correlation of Nirmalkar [17] is the closest to our results. However, coefficients in this correlation are represented as a table, and, therefore, not smooth. Whereas the correlation derived in this paper seems closer to our data.

6. CONCLUSIONS

This paper describes systematic modeling of the Herschel–Bulkley fluid flow over a sphere in a wide range of Reynolds numbers, power indices, and Bingham numbers. Modeling results show the influence of plastic effects on the flow structure around the sphere and the drag at moderate Reynolds numbers. The drag in plastic fluid is higher than in fluid with no yield and with the same viscosity. However, when the Reynolds number increases, the difference in the drag force decreases. At the same time, in non-Newtonian fluid, the influence of the Reynolds number on kinematic and dynamic characteristics of the

flow is weaker than in Newtonian fluid. This influence weakens with the deviation of rheological fluid properties from Newtonian, which, in the particular case of the fluids with yield, are related with plastic effects. In particular, if plastic effects dominate in the flow, which is possible at high values of yield and/or low flow rate, the drag is practically independent of the Reynolds number.

Based on the numerical results, a correlation for the drag has been developed, which takes into account the dependence on all parameters characterizing the flow. Numerical parameters of the developed dependence are such that they ensure good approximation for the general case of the Herschel–Bulkley fluid and for the particular cases of the power law fluid and Bingham fluid. The maximum deviation of the developed correlation from the calculated data in the entire range of parameters is about 5%. In spite of the fact that this correlation works for a wide range of input parameters (power indices $0.3 \le n \le 1$; Reynolds numbers $0 < \mathrm{Re} \le 200$; Bingham numbers $0 \le Bn \le 100$), it should be noted that there are some limits to its applicability. First of all, this correlation has been obtained for the model Herschel–Bulkley fluid, so one must evaluate if it adequately describes the flows of real fluids. In addition, the correlation provided in this paper is based on the results of modeling laminar flows for the steady 2D case. In this case, it is impossible to take into account development of the periodic nonsteady flow that occurs during the laminar-turbulent transition at fairly high Reynolds numbers, as well as the aspects related to stability of real flows. Finally, in the case under consideration here, the fluid flow is unbounded and uniform. It does not include flow shearing induced by external factors. However, the presence of the external shear rate or external stress in the flow of non-Newtonian fluids may lead to changes in effective viscosity and/or changes in the boundaries of the liquid regions (for fluids with yield).

This correlation could be used in various engineering applications where one needs to find the established sedimentation rate of the solid phase in non-Newtonian viscous fluids. However, it is necessary for the concentration of solid particles to remain fairly small, because this correlation does not take into account perturbations brought to the flow by neighboring particles. Nonetheless, as it was shown, with the increase of non-Newtonian properties of the fluid, the influence of the particle on the flow weakens, and thus, the correlation still works at higher concentrations.

ACKNOWLEDGMENTS

The authors thank management of Baker Hughes for permission to publish this paper and personally R. May for valuable comments and suggestions, related to this paper.

REFERENCES

1. Clift, R., Grace, J.R., and Weber, M.E., *Bubbles, Drops and Particles*, New York: Academic Press, 1978.
2. Michaelides, E.E., *Particles, Bubbles and Drops, Their Motion, Heat and Mass Transfer*, World Sci. Publ., 2006.
3. Podryabinkin, E.V. and Rudyak, V.Ya., Moment and Forces Exerted on the Inner Cylinder in Eccentric Annular Flow, *J. Eng. Therm.*, 2011, vol. 20, no. 3, pp. 320–328.
4. Podryabinkin, E., Gavrilov, A., Rudyak, V., and May, R., Detailed Modeling of Drilling Fluid Flow in a Wellbore Annulus While Drilling, *Can. Energy Technol. Innov.*, 2014, vol. 1, no. 5, pp. 27–36.
5. Barnes, H.A. and Walters, K., The Yield Stress Myth?, *Rheol. Acta.*, 1985, vol. 24, pp. 323–326.
6. Chhabra, R., *Bubbles, Drops, and Particles in Non-Newtonian Fluids*, 2nd ed., Taylor & Francis Group, LLC, 2007.
7. Beris, A.N., Tsamopoulos, J.A., Armstrong, R.C., and Brown, R.A., Creeping Motion of a Sphere through a Bingham Plastic, *J. Fluid Mech.*, 1985, vol. 158, pp. 219–244.
8. Blackery, J. and Mitsoulis, E., Creeping Motion of a Sphere in Tubes Filled with a Bingham Plastic Material, *J. Non-Newt. Fluid Mech.*, 1997, no. 70, pp. 59–77.
9. Liu, B.T., Muller, S.J., and Denn, M.M., Convergence of a Regularization Method for Creeping Flow of a Bingham Material about a Rigid Sphere, *J. Non-Newt. Fluid Mech.*, 2002, no. 102, pp. 179–191.
10. Tripathi, A., Chhabra, R.P., and Sundararajan, T., Power-Law Fluid Flow over Spheroidal Particles, *Ind. Eng. Chem. Res.*, 1994, no. 33, pp. 403–410.
11. Tripathi, A. and Chhabra, R.P., Drag on Spheroidal Particles Iin Dilatant Fluids, *AIChE. J.*, 1995, no. 41, pp. 728–731.
12. Graham, D.I. and Jones, T.E.R., Settling and Transport of Spherical Particles in Power Law Fluids at Finite Reynolds Number, *J. Non-Newt. Fluid Mech.*, 1994, no. 54, pp. 465–488.
13. Dhole, S.D., Chhabra, R.P., and Eswaran, V., Flow of Power-Law Fluids Past a Sphere at Intermediate Reynolds Numbers, *Ind. Eng. Chem. Res.*, 2006, no. 45, pp. 4773–4781.

14. Beaulne, M. and Mitsoulis, E., Creeping Motion of a Sphere in Tubes Filled with Herschel–Bulkley Fluids, *J. Non-Newt. Fluid Mech.*, 1997, no. 72, pp. 55–71.
15. Song, D., Gupta, R.K., and Chhabra, R.P., Wall Effects on a Sphere Falling in Quiescent Power Law Fluids in Cylindrical Tubes, *Ind. Eng. Chem. Res.*, 2009, vol. 48, pp. 5845–5856.
16. Nirmalkar, N., Chhabra, R.P., and Poole, R.J., Numerical Predictions of Momentum and Heat Transfer Characteristics from a Heated Sphere in Yield-Stress Fluids, *Ind. Eng. Chem. Res.*, 2013, vol. 52, pp. 6848–6861.
17. Nirmalkar, N., Chhabra, R.P., and Poole, R.J., Effect of Shear-Thinning Behavior on Heat Transfer from a Heated Sphere in Yield-Stress Fluids, *Ind. Eng. Chem. Res.*, 2013, vol. 52, pp. 13490–13504.
18. Rudyak, V.Ya., Minakov, A.V., Gavrilov, A.A., and Dekterev, A.A., Application of New Numerical Algorithm of Solving the Navier–Stokes Equations for Modeling the Work of a Viscometer of the Physical Pendulum Type, *Thermophys. Aeromech.*, 2008, vol. 15, no. 2, pp. 333–345.
19. Gavrilov, A.A., Minakov, A.V., Dekterev, A.A., and Rudyak, V.Ya., Numerical Algorithm for Modeling Flows through the Eccentric Annulus, *Sib. Zh. Ind. Mat.*, 2010, vol. 13, no. 4(44), pp. 3–14.
20. Papanastasiou, T.C., Flow of Materials with Yield, *J. Rheology*, 1987, vol. 31(5), pp. 385–404.
21. Schiller, L. and Nauman, A., Uber die grundlegenden Berechnungen bei der Schwerkraftaufbereitung, *Ver. Dent. Ing.*, 1933, no. 77, pp. 310–320.
22. Gill, P., Murray, W., and Wright, M., *Practical Optimization*, Academic Press, 1997.
23. du Plessis, M.P. and Ansley, R.W., Settling Parameters in Solids Pipelining, *J. Pipeline Div. (ASCE)*, 1967, vol. 93, p. 1.
24. Renaud, M., Mauret, E., and Chhabra, R.P., Power Law Fluid Flow over a Sphere: Average Shear Rate and Drag Coefficient, *Can. J. Chem. Eng.*, 2004, vol. 82, pp. 1066–1070.
25. Ceylan, K., Herdem, S., and Abbasov, T., A Theoretical Model for Estimation of Drag Force in the Flow of Non-Newtonian Fluids around Spherical Solid Particles, *Powder Technol.*, 1999, vol. 102, pp. 286–292.